PCCP

PAPER

View Article Online
View Journal

Cite this: DOI: 10.1039/d5cp03530a

A cyclic ion mobility and DFT study of the structures, isomer space and isomer interconversion of lanthanide bromide clusters, $Ln_xBr_{3x+1}^-$, x = 1–6

Yuto Nakajima,[a] Patrick Weis, *[b] Florian Weigend, *[bc] Marcel Lukanowski,[bc] Fuminori Misaizu [a] and Manfred M. Kappes *[bd]

Cyclic ion mobility–mass spectrometry (IMS–MS) combined with density functional theory (DFT) and trajectory-method simulations were used to study the structures and isomerization of lanthanide bromide cluster anions $Ln_xBr_{3x+1}^-$ ($x \leq 6$, Ln = La–Lu, except Pm). Overall, seventy different species were characterized, revealing two regimes: smaller anions ($x \leq 5$) mostly exhibit rapid isomer interconversion on the sub 10 ms timescale of the experiment while hexamers ($x = 6$) display enhanced rigidity and much slower interconversion dynamics. DFT-predicted minima agree with IMS data, showing essentially ionic bonding with bromide bridging and termination. The isomer space comprises structural motifs that evolve with cluster size from chain and ring topologies to compact three-dimensional frameworks at $x = 6$. Lanthanide contraction shifts relative isomer stabilities which typically leads to systematic structure changes across the Ln series. For $Ln_6Br_{19}^-$, at least two long-lived isomers were observed for all lanthanides. Strikingly, $Pr_6Br_{19}^-$ undergoes spontaneous bidirectional interconversion on the experimental timescale, permitting direct measurement of unimolecular rate constants (k_f = 1.8 s^{-1}, k_r = 0.2 s^{-1}) and consequently an equilibrium constant ($K \approx 9$ at 300 K).

Received 12th September 2025,
Accepted 25th November 2025

DOI: 10.1039/d5cp03530a

rsc.li/pccp

1. Introduction

Thermally activated interconversion of structural isomers and the associated breaking and (re)forming of bonds has been extensively studied in condensed phase using a variety of different physicochemical methods, see *e.g.*: G. Egloff *et al.*,[1] R. E. Fuguitt *et al.*[2] and references therein and Xu *et al.*[3] Investigations of isomer conversion in gas phase are less common due to their added technical complexity. The molecules of interest must typically first be selected from mixtures before isomeric composition can be probed (time-dependently) under conditions ensuring that competing decay processes, *e.g.* fragmentation, remain insignificant. A particularly useful method to study interconversion of charged isomers in gas-phase, established since the 1990s, is the combination of mass spectrometry (MS) with ion mobility spectrometry (IMS). After selection according to their mass-to-charge ratio, relative amounts of isomeric ions can be distinguished according to their collision cross sections (CCS) *via* passing them through a collision cell filled with an inert gas (and measuring the time associated with drift cell passage).[4–6] Today IMS–MS is used routinely to analyse isomer and conformer compositions as well as to study changes induced by collisional annealing.[6–11]

Whether or not two isomeric ions can be resolved by IMS depends not only on their CCS difference and therefore the instrumental resolution, but also on their forward and reverse interconversion rates – which are themselves functions of the internal excitation levels pertaining. An operational criterium is that the time required to determine isomeric composition at the CCS resolution necessary to distinguish the isomers should be significantly shorter than the inverse isomer interconversion rate constant. Only then can two baseline separated isomer peaks be observed in the corresponding mobilograms (which show ion intensity *versus* drift time/CCS). On the other hand, if the inverse interconversion rate constant is much faster than this measurement time, only one sharp peak at the weighted CCS average of the two isomers is observable. For the intermediate situation: if the inverse interconversion rate constant becomes comparable to the measurement time, the corresponding mobilograms show partially resolved isomeric peaks with ion intensity also between the peaks. These phenomena

[a] Department of Chemistry, Graduate School of Science, Tohoku University, Japan
[b] Institute of Physical Chemistry, Karlsruhe Institute of Technology (KIT), Germany. E-mail: patrick.weis@kit.edu, manfred.kappes@kit.edu, florian.weigend@kit.edu
[c] Institute for Quantum Materials and Technologies, Karlsruhe Institute of Technology (KIT), Germany
[d] Institute of Nanotechnology, Karlsruhe Institute of Technology (KIT), Germany

can be quantitatively modelled using the transport theory of reacting ions as developed by Gatland[12] (for atomic ions in different electronic states, initially investigated by IMS without mass selection). Gatland theory was first applied to molecules in an IMS–MS study of alkali halide clusters from which T-dependent forward isomerization rate constants were inferred.[13] Subsequently, some of us also applied this approach to the T-dependent isomer interconversion of small gold cluster cations.[14] More recently the Gatland formalism has also been used to describe the interconversion of various supramolecular conformers[15] as well as conformer change of crown ethers complexed with K^+ atoms.[16]

The recent introduction of next generation commercial IMS–MS instrumentation platforms, *e.g.* with cyclic drift cells, has significantly increased accessible drift time ranges.[17] This has made CCS resolutions (CCS/delta CCS) approaching 1000 routinely available for studies of ions near room temperature. These instruments also offer the possibility of isomer selection, storage and mobility reanalysis which in principle allows to separately probe the rates of forward and reverse isomerization reactions – if they fit into the kinetic window of the apparatus. However, molecular ion systems in which the approach to equilibrium have been directly studied from both sides of an isomerization barrier have yet to be described in gas phase.

In this context we have recently investigated the size dependence of structural isomerism in small lanthanide chloride $Ln_xCl_{3x+1}^-$ clusters held at near room temperature and ranging in size from x = 2–6 – comparing the behaviour for all 14 accessible lanthanide elements, Ln = La···Lu (except Pm). $Ln_xCl_{3x+1}^-$ clusters are subject to the well-known lanthanide contraction, see *e.g.* Jordan,[18] which at a given cluster size turns out to systematically change the relative energies of the lowest lying isomeric structures (in going across the Ln series from the 4f-element with the largest (La^{3+}) to smallest (Lu^{3+}) ionic radius) – oftentimes leading to an inversion of energetic ordering of the lowest two isomers in the respective cluster family. This combined with bonding interactions that are essentially ionic (and therefore spatially isotropic), and with comparatively small isomerization but large fragmentation barriers, leads to interesting phenomenology. We were able to interpret these experimental results with the help of DFT calculations using newly designed polarized effective core potential based triple zeta valence basis sets, lcecp-1-TZVP, developed for 4f-elements.[19] For many of the $Ln_xCl_{3x+1}^-$ clusters with $x \leq 5$ (notably all Ln_2Cl_7, Ln_4Cl_{13} (Gd–Tm) and Ln_5Cl_{16} (Pr and Nd)), the measured arrival time distributions could only be explained by fast interconversion between typically the lowest energy isomers – faster than the experimental timescale needed to resolve their different CCS values and therefore too fast to determine rate constants.[20] By contrast, we observed for all $Ln_6Cl_{19}^-$ clusters two base-line resolved isomers that showed no signs of interconversion even on the longest accessible experimental timescale (>200 ms). Interestingly, however each of the two $Ln_6Cl_{19}^-$ isomers could be individually converted into the other isomer by collisional annealing (after appropriate isomer selection). What's more, the as-prepared isomer ratio could be essentially recovered – following sufficient collisional annealing (involving energization still much below the threshold for dissociation).

In principle, the 5 × 14 different lanthanide chloride cluster anions studied offered two variables with which to tune their isomer interconversion dynamics: cluster size and Ln^{3+} ionic radius. However, this tuning raster turned out to be still too coarse to find a room temperature lanthanide chloride cluster with forward and reverse interconversion rate constants falling into the experimental time window. We speculated that this goal might be achievable by also changing the halide ionic radius and thus the isomer interconversion barrier. Here we present results (*i.e.* IMS–MS experiments and DFT calculations) for the corresponding lanthanide bromide clusters, $Ln_xBr_{3x+1}^-$ (Ln = La···Lu, except Pm; $x \leq 6$) and compare their behaviour to the chlorides. For the smaller clusters, $x \leq 5$, the behaviour is qualitatively the same (analogous isomer space; faster than measurable interconversion between the two lowest energy isomers for most clusters). However, for $Ln_6Br_{19}^-$ we found significant differences: while Ln = Nd–Lu, still show no interconversion on the timescale of the experiment, the early lanthanides interconvert with rates that change measurably along the series La → Ce → Pr. Notably, both the forward and reverse isomer interconversion rate constants of $Pr_6Br_{19}^-$ fall into the experimental time window. Below we present the results and discuss some of the consequences.

2. Experimental and theoretical methods

2.1 Cluster anion formation and ESI mass spectra

Isolated cluster ions were generated by electrospray ionization. For this, solutions of *ca.* 0.05 mmol l^{-1} of $LnBr_3$ (Ln = La–Lu, except Pm) in isopropanol were electrosprayed into a Waters select series cyclic ion mobility mass spectrometer (for a detailed description of the setup and multi-cycle calibration procedure, see[10,17]). In negative ion mode, salt clusters with the composition $Ln_xBr_{3x+1}^-$ ($x \leq 6$) were readily formed. A typical mass spectrum (using $LaBr_3$ as an example) is shown in Fig. 1. Based on observed concentration dependencies, clusters were generated during the spray process itself.

$LaBr_3$ was obtained from Thermo Fisher. $NdBr_3$ and $LuBr_3$ were obtained from ChemPur. The other bromides studied here were made by reacting the respective carbonates or chlorides (obtained from various commercial sources) with an excess of concentrated HBr and evaporating to dryness. The $LnBr_3$ precipitate was dissolved in isopropanol, centrifuged, and diluted to *ca.* 0.05 mmol l^{-1}.

2.2 Ion mobility measurements

All ion mobility experiments were performed in a Waters select series cyclic ion mobility mass spectrometer that comprises an ESI source, a quadrupole mass filter, a radio-frequency ion trap (PreTrap), a T-wave array, a cyclic travelling wave ion mobility cell (cIMS) and high resolution time-of-flight mass

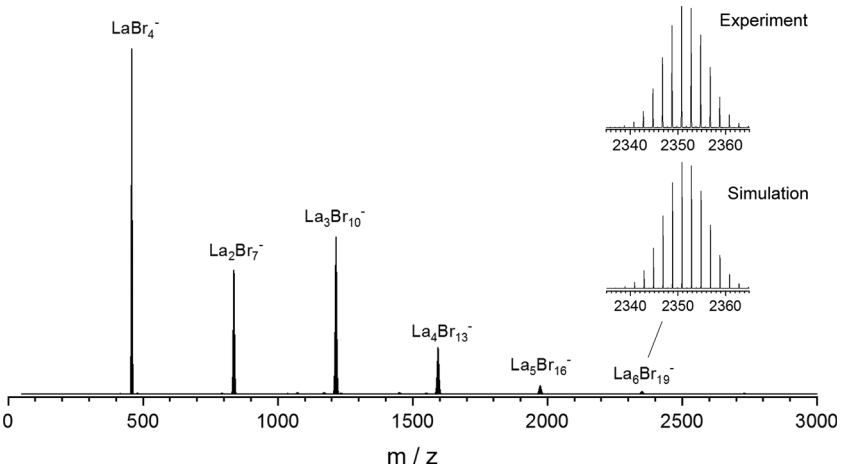

Fig. 1 Overview ESI mass spectrum of a solution of 0.05 mmol l^{-1} $LaBr_3$ in isopropanol, negative ion mode. The other $LnBr_3$ solutions showed analogous overview mass spectra. The IMS measurements reported below were performed under mass-selective conditions, *i.e.* results are specific to $Ln_xBr_{3x+1}^-$, x = 1–6, throughout.

spectrometer (ToF). The T-wave array is a switching device that either directs the ions forward to the ToF (for MS-only experiments), sideways into the cIMS for an arbitrary number of cycles (for IMS experiments, the resolution increases with the number of cycles chosen), or back into the PreTrap (for IMS^n experiments), see instrumental setup schematics in.[17] The respective steps can be combined depending on the experimental needs. The ion mobility cell is filled with 1.7 mbar of nitrogen as drift gas and operated at room temperature.

For the ion mobility measurements, the respective species were isolated in the quadrupole mass filter prior to the cyclic ion mobility cell.[10,17] This procedure effectively removes any contaminations due to fragmentation in the mobilograms: otherwise upon injection, larger clusters can undergo fragmentation by $LnBr_3$ loss, into the respective mass channel probed. With mass selection before the cell and mobility analysis performed at the precursor ion mass only, this contamination is eliminated.

2.3 Quantum chemical calculations

The energy surfaces of $Ln_xBr_{3x+1}^-$, Ln = La–Lu and x = 2–6, were investigated with TURBOMOLE.[21] First, a genetic algorithm procedure[22] available within the program package was performed for each x and each Ln, scanning a total of more than 5000 isomers for each Ln using the PBE functional[23] with the 28-mwb 3s3p1d basis[24] (as specified in Section 12 of the SI) and a corresponding energy-adjusted ECP[25] for Br; for lanthanides, large-core-f^{x-1} effective core potentials[26,27] (which cover, for example, the inner shells plus two f electrons for Pr) were used together with newly designed error-balanced polarized double zeta basis sets[19] lcecp-1-SVP. For a given x, the structure with the lowest energy and all energetically following structures up to approx. 100 kJ mol^{-1} were collected for all Ln and then redundant structures were removed. In detail, for each Ln and x, structures with energies agreeing within $\sim$10 kJ mol^{-1} were compared by visual inspection. In this way, typically about three isomers for each cluster size were obtained. These structure sets were optimized for all Ln at higher level, *i.e.* with the functional and the ECPs specified above, but now employing def2-TZVP bases for Br and lcecp-1-TZVP bases for the lanthanides[19,28] (specified in Section S11 of the SI), and furthermore fine grids (grid size 5)[29] as well as tight energy convergence (energy change between iterations below 10^{-9} E_h). The optimized structures were symmetrized to the highest symmetry, which was reduced again in the case of imaginary frequencies until their disappearance. Additionally, vibration spectra were calculated for each species, which yielded real frequencies throughout. These were used to calculate the free energy within the harmonic oscillator rigid rotor model at 0 and 300 K. Finally, the transition paths between the lowest and second lowest isomers were optimized using a generalized Newton method[30] at the higher level (see above), and the identified maxima were finally optimized using the corresponding tool in TURBOMOLE with standard options.

2.4 CCS calculations: calibration of the Lennard-Jones parameters

Candidate structures predicted by quantum chemical methods such as DFT can be ruled out or confirmed by comparing their calculated CCS (termed $^{theo}CCS_{N2}$) with experimental values, $^{TW}CCS_{N2}$ (the prefix TW indicates that the measurements were performed in a travelling wave device, the suffix N2 indicates the drift gas, nitrogen).[31] For the CCS calculations, we use the trajectory method as implemented in IMoS1.09.[32,33] In this method, the interaction between the drifting ion and the nitrogen buffer gas is modelled by a combination of Lennard-Jones, ion-induced dipole and ion–quadrupole interactions with element specific Lennard-Jones parameters. However, only the parameters for C, H, O, N and F are optimized in IMoS, all other elements are treated with default values, σ = 3.5 Å and ε = 2.6 meV. In our previous study on lanthanide chloride clusters,[20] we optimized the parameters for Ln (σ_{Ln} = 3.0 Å

and ε_{Ln} = 2.6 meV, keeping the same parameter for all lanthanides) and Cl (σ_{Cl} = 3.87 Å and ε_{Cl} = 2.6 meV). Test calculations with these parameters for the $Ln_xBr_{3x+1}^-$ clusters show that the calculations underestimate the CCS – as expected, since the ionic radius of the bromide anion is larger than chloride (1.96 Å *vs.* 1.81 Å).[34] Keeping this 0.15 Å difference, we set σ_{Br} = 4.02 Å and adjusted ε_{Br} to closely match the experimental CCS. As "calibration points" we chose a small and a large cluster with well-known structures based on the DFT calculations (see below). Our choice fell on the smallest anion, $LuBr_4^-$ (a tetrahedron), and $Lu_5Br_{16}^-$ because here, according to the calculations, only one isomer is relevant since it is clearly favoured by more than 70 kJ mol^{-1} relative to the next lowest isomer (see below). The best fitting ε_{Br} that we obtain is ε_{Br} = 3.12 meV, with this value we slightly underestimate the experimental CCS for $LnBr_4^-$ (by 0.8%) while we overestimate it by 0.7% for $Ln_5Br_{16}^-$, similar to our findings for the Ln–chloride clusters.[20] As in this previous study we calculate the partial charges on each atom with the ESP-fit.[35] The non-perfect fit obtained reflects the limitations inherent in the simple picture of Lennard-Jones-type interactions with element specific parameters between buffer gas and drifting ion and localized partial charges. For the following we should keep in mind, that based on our calibration, we expect a slight underestimation of the experimental CCS for small clusters ($LnBr_4^-$, $Ln_2Br_7^-$), and a slight overestimation (*ca.* 1%) for large clusters ($Ln_5Br_{16}^-$, $Ln_6Br_{19}^-$). The intermediate sizes ($Ln_3Br_{10}^-$, $Ln_4Br_{13}^-$) should match within 0.5% or better.

3. Results and discussion

3.1 Mobilograms

Typical mobilograms (arrival time distributions obtained for 10 cycles) are shown in Fig. 2 for all $Ln_xBr_{3x+1}^-$ studied. In most cases single, essentially Gaussian peaks are observed. The $Ln_6Br_{19}^-$ clusters are an exception, where in most cases two peaks are observed. Based on mobilograms for 1, 5 and 10 cycles we determined the drift time per cycle for each species by fitting Gaussians to the respective mobilograms. This multi-cycle procedure efficiently removes end effects such as transfer times to the time-of-flight mass spectrometer and thus leads to highly reproducible results.[10] In a second step, collision cross sections (termed $^{TW}CCS_{N2}$ in the following) were obtained by calibration with highly accurate drift-tube based CCS values for the set of ions in Agilent tune mix.[36] For details of the calibration procedure see ref. 10. The resulting $^{TW}CCS_{N2}$ are summarized in Table 1 and Fig. 3, the relative statistical error (standard deviation of the mean for at least three separate measurements) is in all cases below 0.5%. The corresponding $^{TW}CCS_{N2}$ of the chlorides $Ln_xCl_{3x+1}^-$ are shown in Fig. S1 and Table S1 for comparison.

3.2 Structural inferences

Next, we compared predicted ^{theo}CCS values (based on structural models from our DFT calculations and corresponding trajectory method simulations) with calibrated collision cross sections, $^{TW}CCS_{N2}$, so as to make inferences concerning structures, isomer composition and isomer interconversion – for each x (starting with the smallest species studied).

$LnBr_4^-$. The experimental $^{TW}CCS_{N2}$ of $LnBr_4^-$ decrease monotonically from 127.6 Å^2 (for $LaBr_4^-$) to 123.2 Å^2 (for $LuBr_4^-$). This finding parallels our observation for the respective chlorides where we observed a decrease from 116.8 Å^2 to 113.1 Å^2. The *ca.* 9% CCS-difference (see Table S2) reflects the larger ion radius of Br^- *vs.* Cl^-. The calculated $^{theo}CCS_{N2}$, based on the DFT-optimized structures and the trajectory method (with σ_{Ln} = 3.0 Å, ε_{Ln} = 2.6 meV, σ_{Br} = 4.02 Å and ε_{Br} = 3.12 meV, see above) reproduce the trend of decreasing CCS from La (125.5 Å^2) to Lu (122.2 Å^2) but systematically underestimate the experimental values by 1.6% (La) to 0.8% (Lu, one of our calibration points). Note that we use the same Lennard Jones parameters for all lanthanides – varying them within reasonable limits (while keeping the respective DFT derived Ln–Br bond lengths constant) does not change the calculated cross sections significantly since the central metal atom is basically shielded by the four surrounding bromides. In effect, in the trajectory calculations the buffer gas (nitrogen) molecule interacts with the bromide LJ-potential only (Fig. 4).

$Ln_2Br_7^-$. For the dimers, $Ln_2Br_7^-$, we observe a monotonic $^{TW}CCS_{N2}$ decrease from 164.7 Å^2 for $La_2Br_7^-$ to 156.4 Å^2 for $Yb_2Br_7^-$. $Lu_2Br_7^-$ has a slightly larger $^{TW}CCS_{N2}$ of 157.2 Å^2. According to our DFT geometry optimizations, there are three isomers to be considered: the first, isomer **A**, consists of three bridging bromides (μ_2-Br) and two terminal bromides on each lanthanide (Fig. 5, red data points and corresponding structural schematic). The second isomer, **B**, consists of only two bridging bromides (μ_2-Br) and two terminal bromides on one of the lanthanides and three on the other (Fig. 5, green data points). The third isomer, **C**, has three μ_2-Br as for **A**, but three terminal bromides on one of the lanthanide atoms and one on the other (Fig. 5, blue data points). The calculated $^{theo}CCS_{N2}$ are only *ca.* 1% smaller than the experimental values for **A** and agree even better for **C**, see Fig. 5(a). The **B** isomers have calculated $^{theo}CCS_{N2}$ that are between 3% and 4% higher than the experimental values. The relative energies (0 K, ZPE not included) clearly disfavour isomers C – they are always at least 20 kJ mol^{-1} above the respective global minima (Fig. 5(b)). The isomers **A** and **B** however, are very close in energy: **A** is favoured for the early lanthanides (La: 5.5 kJ mol^{-1}), while **B** is favoured for the late lanthanides (Lu: 2.7 kJ mol^{-1}). These differences, ΔE, refer to the electronic energies, *i.e.* at 0 K, without zero-point energies. In a second step, we also calculated the free energy differences at 300 K, ΔG_{300}, taking into account harmonic vibrational frequencies, see Fig. 5(c). It turns out, that their impact is rather small, *i.e.* variations of ΔE and ΔG_{300} between pairs of isomers are generally similar for all Ln. Note however, that we often found lowest harmonic vibrational frequencies to be below 10 cm^{-1}, reflecting the low reduced masses and relatively floppy structures of $Ln_xBr_{3x+1}^-$. In particular these low frequency modes are in fact likely to be highly anharmonic and are therefore difficult to accurately calculate. Thus, for the

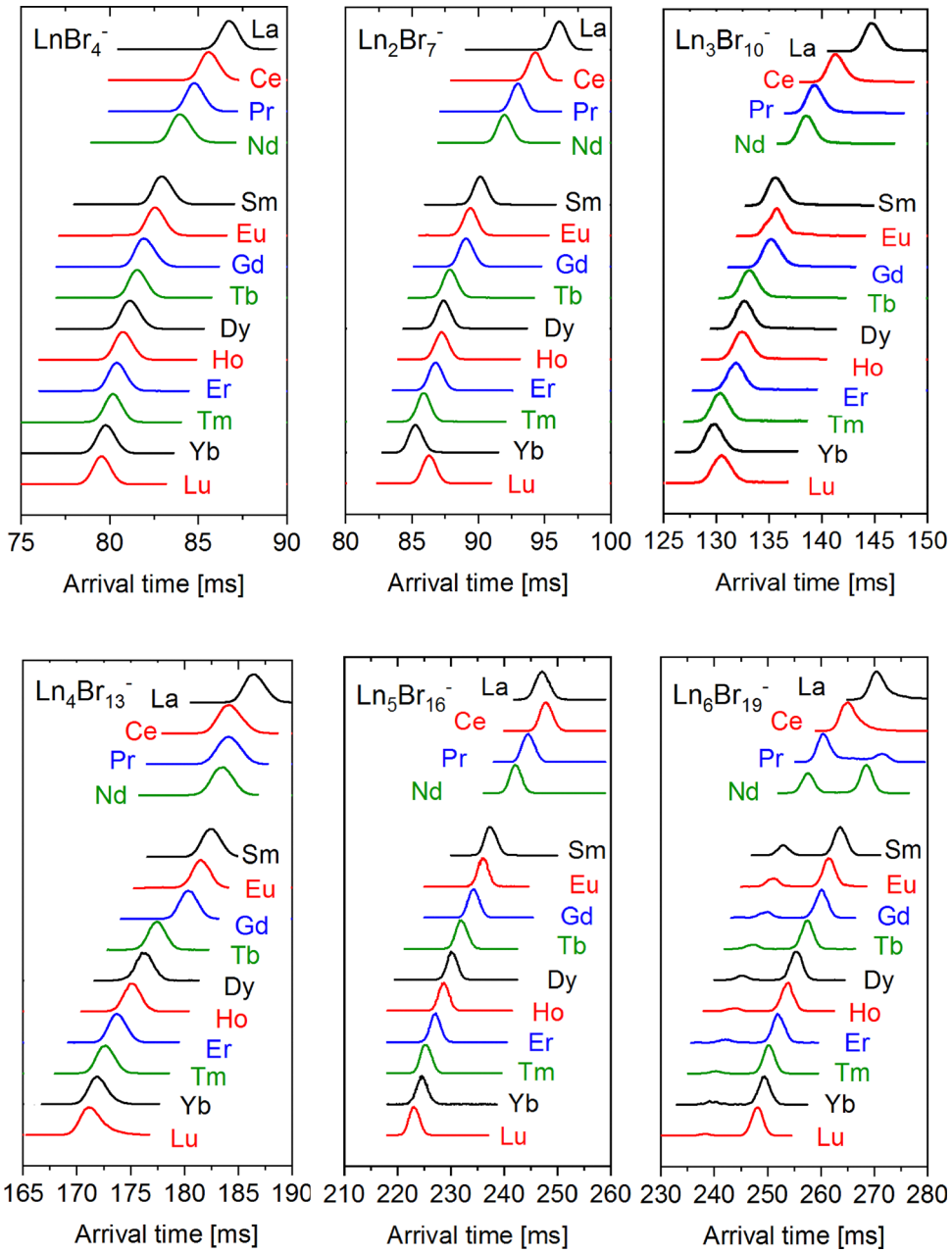

Fig. 2 Typical arrival time distributions of $Ln_xBr_{3x+1}^-$ anions after 10 cycles (for given x = 1–6 as indicated). A travelling wave (TW) speed of 375 m s^{-1} was used in all cases. For x = 2–6, a TW height of 18 V was used. $LnBr_4^-$ (x = 1) was measured with a TW height of 14 V (peak height of the travelling wave that propagates the ions through the cell). At 18 V the large mobility of this ion causes undesirable "surfing" on the TW rather than CCS dependent separation. Note, that a second isomer of $La_6Br_{19}^-$ is observable in experiments with less than 5 cycles only (*cf.* Table 1, Fig. 3 and Fig. 10(a)).

following we choose to restrict our discussion to the differences in electronic energy ΔE.

It is clear that isomers **A** and **B** are energetically close and – assuming thermodynamic equilibrium – should be present in comparable intensities. Furthermore, since their calculated CCS differ by *ca.* 4% they should be easily resolvable in our instrument – already after a few cycles of separation. However, we observe in all cases only one sharp peak, see Fig. 2. This could mean that either only isomer **A** is present (it agrees much better with the experimental CCS than isomer **B**) or that both isomers are quickly interconverting, much faster than our experimental timescale (10 ms). Therefore, we also calculated the interconversion barrier between **A** and **B** and find it to be very low, below 10 kJ mol^{-1} (see Fig. 5(d)). As the experimental $^{TW}CCS_{N2}$ values are in between the $^{theo}CCS_{N2}$ values calculated for **A** and **B**, we favour the fast interconversion scenario – consistent with our previous inferences for $Ln_2Cl_7^-$. For a simulation of the peak shape as function of the interconversion rate see Fig. S8. Isomer **C** might also be contributing but only in small amounts since it is energetically strongly disfavoured.

Table 1 Experimental travelling wave $^{TW}CCS_{N2}$ values for $Ln_xBr_{3x+1}^-$ anions (in Å^2). For $Ln_6Br_{19}^-$ we observe two peaks. The relative intensities of the two isomers are given in brackets. The statistical error (standard deviation of the mean) of the $^{TW}CCS_{N2}$ is below 0.5%

	$LnBr_4^-$	$Ln_2Br_7^-$	$Ln_3Br_{10}^-$	$Ln_4Br_{13}^-$	$Ln_5Br_{16}^-$	$Ln_6Br_{19}^-$	
La	127.6	164.7	195.7	218.8	248.7	259.1 (100%)[a]	272.6 (<5%)[a]
Ce	127.1	163.4	193.6	217.6	248.9	256.6 (100%)[a]	
Pr	126.9	162.3	191.9	217.3	247.3	254.6 (79%)[a]	259.5 (21%)[a]
Nd	126.1	161.7	191.4	217.0	246.2	253.1 (46%)	258.1 (54%)
Pm							
Sm	125.7	160.4	190.1	216.6	244.1	250.9 (26%)	255.9 (74%)
Eu	125.4	159.7	189.3	216.0	243.4	250.2 (27%)	255.0 (73%)
Gd	125.3	159.6	189.5	215.5	242.6	249.6 (19%)	254.4 (81%)
Tb	124.9	159.0	188.5	214.4	241.5	248.4 (16%)	253.3 (84%)
Dy	124.5	158.0	187.5	213.4	240.4	248.0 (13%)	252.7 (87%)
Ho	124.1	157.8	187.4	212.9	239.6	246.3 (11%)	251.3 (89%)
Er	124.0	157.6	186.7	212.5	238.7	245.6 (10%)	250.3 (90%)
Tm	123.7	156.9	185.5	211.9	237.9	244.8 (8%)	249.6 (92%)
Yb	123.5	156.4	184.4	211.0	237.4	244.1 (8%)	248.9 (92%)
Lu	123.2	157.2	184.0	210.7	237.0	243.8 (7%)	248.5 (93%)

[a] Intensity ratio varies with the number of cycles (see text). Note that the second peak of $La_6Br_{19}^-$ with <5% intensity quickly decreases with the number of cycles (see Fig. 10(a)), therefore it is not visible in the 10 cycles measurements shown in Fig. 2.

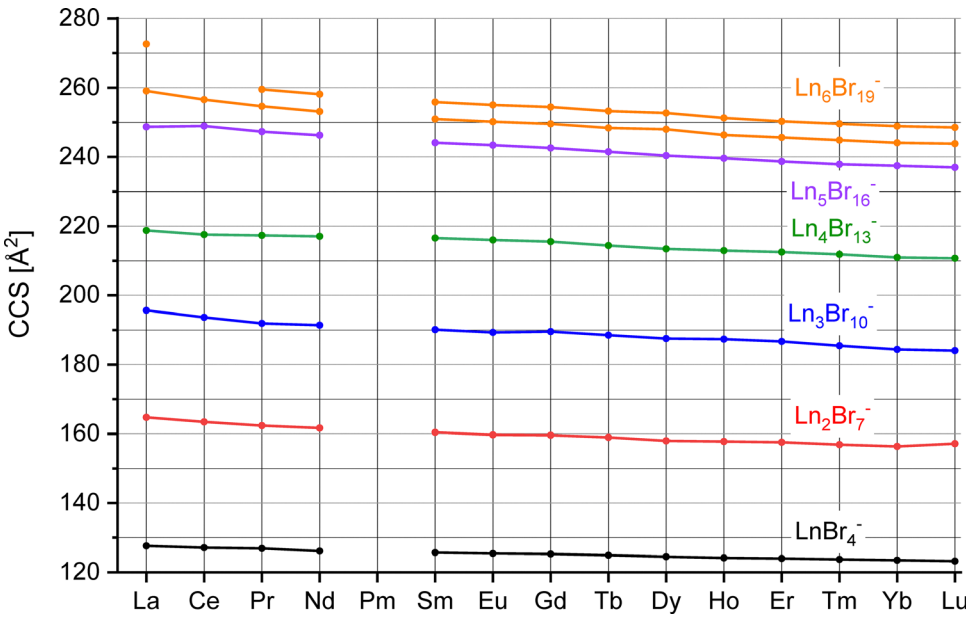

Fig. 3 Experimental collision cross sections $^{TW}CCS_{N2}$ of $Ln_xBr_{3x+1}^-$, x = 1–6, Ln = La–Lu except Pm (see Table 1). The relative statistical error (standard deviation of the mean) is in all cases below 0.5% corresponding roughly to the size of the data points.

$Ln_3Br_{10}^-$. For all of the trimers we always observe one sharp peak in the arrival time distributions (see Fig. 2) and an essentially monotonic $^{TW}CCS_{N2}$ decrease from 195.7 Å^2 for $La_3Br_{10}^-$ to 184.0 Å^2 for $Lu_3Br_{10}^-$, *i.e.* by 6% (see Fig. 6(a), black circles and error bars). In the calculations we find three relevant isomers **A**, **B** and **C**. Isomer **A** consists of a Ln_3Br_3-ring with 3 μ_2-Br and two central bromides, above and below the ring, and coordinated to all three Ln-atoms (μ_3-Br). The remaining 5 bromides are terminal, *i.e.* each is coordinated to only one Ln-atom, resulting in C_{2v} symmetry, see Fig. 6(a). The next isomer, **B**, with C_{3v} symmetry is a variant thereof, with one central (μ_3-Br) and six terminal bromides. It is between 23 kJ mol^{-1} (Lu) and 19 kJ mol^{-1} (La) higher in energy, see Fig. 6(b). The barrier height between **A** and **B** is *ca.* 28 kJ mol^{-1} for all Ln (with isomer **A** as reference), see Fig. 6(c) and Fig. S2, which is possibly low enough for interconversion on the timescale of the experiment. The third isomer **C** that we find is a linear chain with six bridging (μ_2-Br) and four terminal bromides. It is also energetically disfavoured, between 25 and 18 kJ mol^{-1} above isomer **A**. The $^{theo}CCS_{N2}$ of **A** agree with the experimental $^{TW}CCS_{N2}$ within the experimental uncertainty (0.5%), while the $^{theo}CCS_{N2}$ of **B** and **C** are 2.5–5% above the experiment. Based on these results, it is clear that isomer **A** is the dominant species contributing to the experimental observation, *i.e.* we do not need to invoke fast isomerization in this system (but cannot completely exclude it).

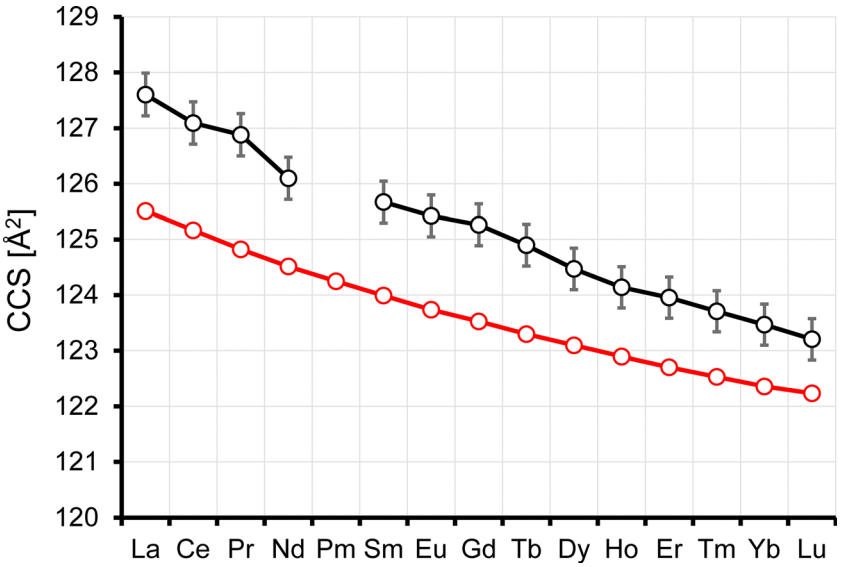

Fig. 4 Experimental (black circles with error bars, $^{TW}CCS_{N2}$) and calculated (red circles, $^{theo}CCS_{N2}$) collision cross sections for $LnBr_4^-$.

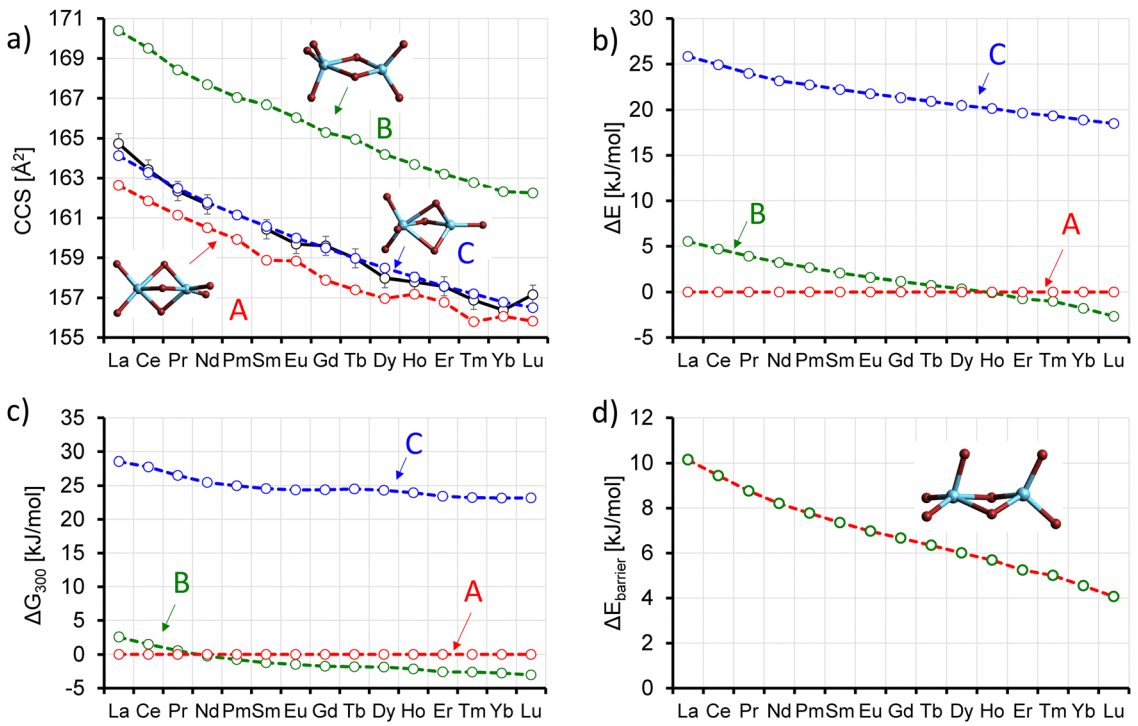

Fig. 5 (a) Experimental (black circles with error bars, $^{TW}CCS_{N2}$) and calculated (red, blue and green circles, $^{theo}CCS_{N2}$) collision cross sections for the three calculated isomers **A**, **B**, **C** of $Ln_2Br_7^-$. (b) Calculated (electronic) energy differences, taking isomers **A** as references, zero-point energies not included. (c) Free energy differences, calculated within the harmonic oscillator model, taking isomers **A** as references. (d) Transition state and energy barriers between isomers **A** and **B**, taking isomers **A** as references.

$Ln_4Br_{13}^-$. For all of the tetramers, we again observe only one sharp peak in all cases and a monotonic $^{TW}CCS_{N2}$ decrease, from 218.8 Å^2 for $La_4Br_{13}^-$ to 210.7 Å^2 for $Lu_4Br_{13}^-$, see Fig. 7(a). This corresponds to a *ca.* 3.7% reduction in average size along the series which is significantly less than the 6% decrease observed for $Ln_3Br_{10}^-$ and suggests an overall structural transition.

In the lowest energy isomer that was found for $La_4Br_{13}^-$ by DFT, the four La atoms form a ring structure with two bromides on each edge (8 μ_2-Br), four terminal bromides, a central bromide (1 μ_4-Br) and C_{4v}-symmetry (Fig. 7(a), structure **A**). Its calculated $^{theo}CCS_{N2}$ of 219.1 Å^2 perfectly matches the experimental value of 218.8 Å^2. For La, this isomer is preferred by 3 kJ mol^{-1} over **B**, where the La atoms form a butterfly

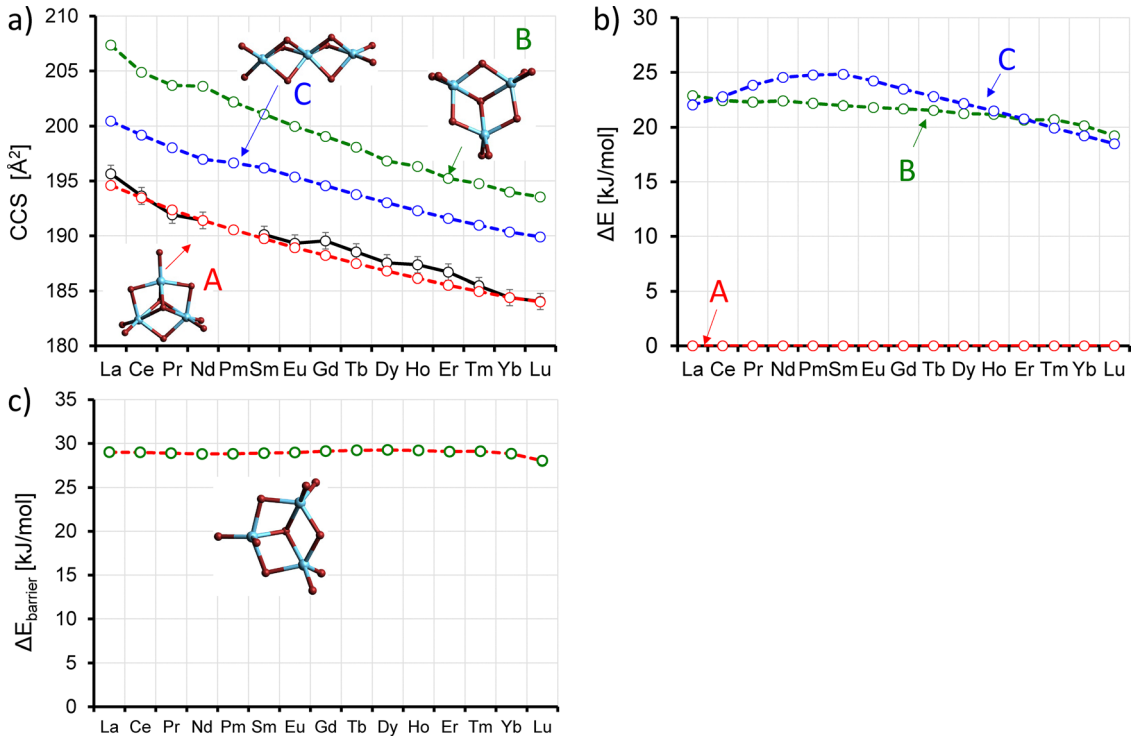

Fig. 6 (a) Experimental (black circles with error bars, $^{TW}CCS_{N2}$) and calculated (red, blue and green circles, $^{theo}CCS_{N2}$) collision cross sections for the three calculated isomers **A**, **B**, **C** of $Ln_3Br_{10}^-$. (b) Calculated (electronic) energy differences, taking isomers **A** as references, zero-point energies not included. (c) Transition state and energy barriers between A and B, taking isomers A as references.

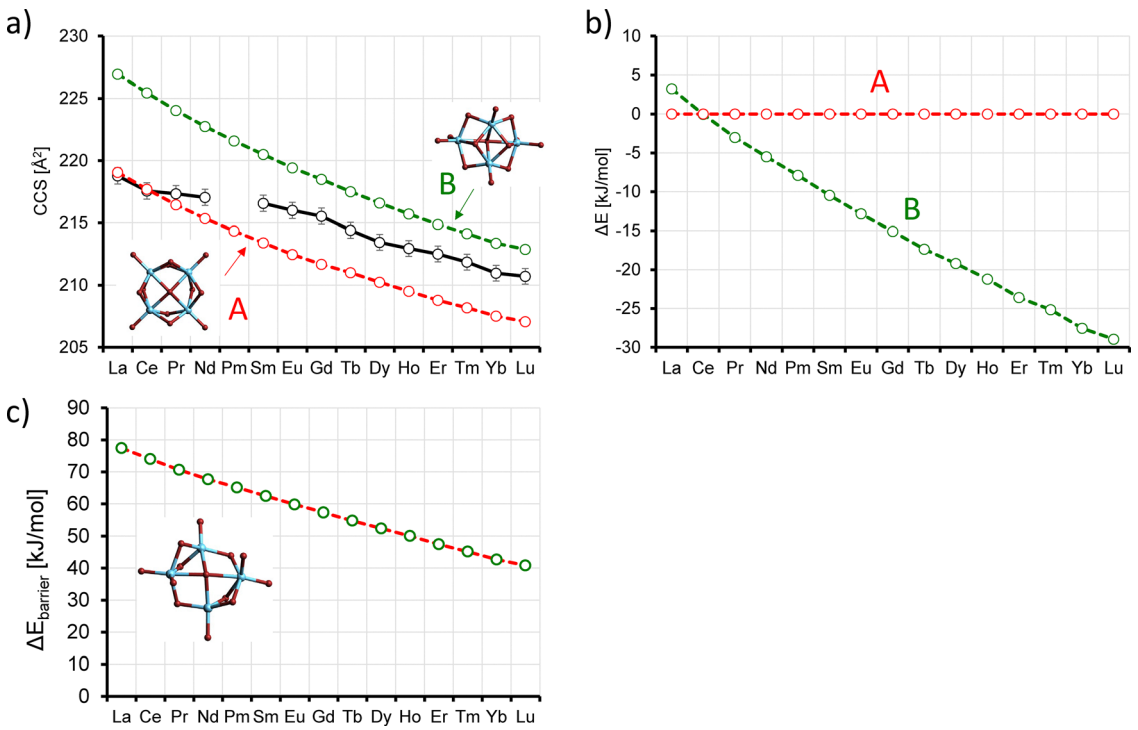

Fig. 7 (a) Experimental (black circles with error bars, $^{TW}CCS_{N2}$) and calculated (red and green circles, $^{theo}CCS_{N2}$) collision cross sections for the two calculated low energy isomers **A** and **B** of $Ln_4Br_{13}^-$. (b) Calculated (electronic) energy differences, taking isomers **A** as reference, zero-point energies not included. (c) Calculated barrier heights between the isomers **A** and **B** with isomer **A** as reference.

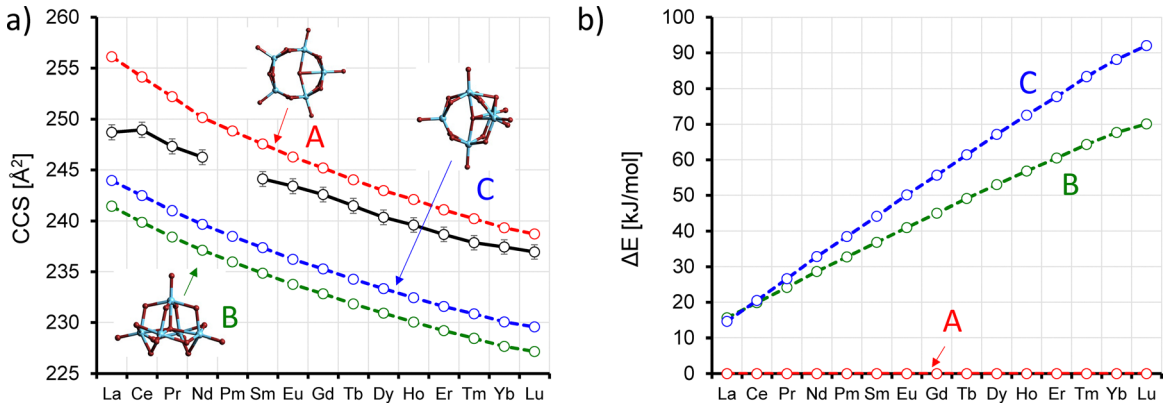

Fig. 8 (a) Experimental (black circles with error bars, $^{TW}CCS_{N2}$) and calculated (red, blue and green circles, $^{theo}CCS_{N2}$) collision cross sections for the three calculated isomers **A**, **B**, **C** of $Ln_5Br_{16}^-$. (b) Calculated (electronic) energy differences, taking isomers **A** as reference, zero-point energies not included.

structure, with edges and planes bridged by bromides (1 μ_4-Br, 2 μ_3-Br, 4 μ_2-Br), and additionally two terminal Br each at two of the La atoms and one each at the two others. For all other lanthanides, isomer **B** is increasingly favoured over **A**, by up to 29 kJ mol^{-1} (for $Lu_4Br_{13}^-$), see Fig. 7(b). The $^{theo}CCS_{N2}$ of **B** are always 3–4% larger than the corresponding values for **A**, see Fig. 7(a). We also find two closely related isomers with C_2 symmetry, **C** and **D**. However, they are more than 40 kJ mol^{-1} above the respective lowest energy isomer (**A** or **B**) and can be ruled out.

If we compare experiment and calculation, we find that the experimentally observed 3.7% CCS decrease between La and Lu cannot be explained by a single isomer. For both **A** and **B**, the decrease is much larger (5.5% and 6.2%, respectively). Furthermore, we find that for the early lanthanides $^{TW}CCS_{N2}$ and the calculated $^{theo}CCS_{N2}$ of **A** closely match while for the late lanthanides, the experimental values approach $^{theo}CCS_{N2}$ predicted for **B**. On the other hand, we always observe one sharp peak in the corresponding arrival time distributions (see Fig. 2), Therefore, we conclude that we observe a dynamic equilibrium between **A** and **B** with quick interconversion on the 100 ms timescale (otherwise we should observe a peak broadening, which we do not see. For a simulation of the peak shape as function of the interconversion rate see Fig. S8). This is associated with an increasing share of **B** in going from La to Lu. We note in passing, that the calculated barrier height between the isomers decreases form 77 kJ mol^{-1} to 41 kJ mol^{-1} (when referenced to **A**) in going from left to right in the lanthanide series (or remains constant at *ca.* 75 kJ mol^{-1} when referenced to **B**), see Fig. 7(c).

$Ln_5Br_{16}^-$. The $^{TW}CCS_{N2}$ of $La_5Br_{16}^-$ and $Ce_5Br_{16}^-$ are essentially identical, 248.7 Å^2 and 248.9 Å^2 respectively. For the rest of the series $^{TW}CCS_{N2}$ decreases from 247.3 Å^2 for $Pr_5Br_{16}^-$ to 237.0 Å^2 for $Lu_5Br_{16}^-$, see Table 1 and Fig. 8(a). In the calculations we find three relevant isomers: a ring-type isomer **A** with C_{2v} symmetry is always lowest in energy (1 μ_3-Br, 10 μ_2-Br, 5 terminal). Two other more compact isomers (**B** and **C**, with C_{2v} and C_s symmetry, respectively) are for La only 15 kJ mol^{-1} higher in energy than **A**. This energy difference quickly increases and for Lu both **B** and **C** are strongly disfavoured by 70 and 92 kJ mol^{-1} respectively, see Fig. 8(b). Based on the calculations it is clear that only **A** is relevant for the late lanthanides. For this reason, we have chosen $Lu_5Br_{16}^-$ as a second calibration point to adjust the LJ-parameters used in the trajectory calculations (see above). Consequently, experimental and theoretical CCS (for **A**) closely match (within 1%) for the late lanthanides, while $^{theo}CCS_{N2}$ for **B** and **C** are 4% and 3% smaller than $^{TW}CCS_{N2}$. For the early lanthanides, with decreasing energy difference the experimental CCS approaches the values for **B** and **C**. The flattening of the $^{TW}CCS_{N2}$ curve with almost identical values for $La_5Br_{16}^-$ and $Ce_5Br_{16}^-$ is in line with larger fractions of isomers **B** and/or **C** being present for La. Since we observe in all cases only one sharp peak in the mobilograms, we again reach the conclusion that a dynamic equilibrium with quick interconversion must be present.

For comparison, in the case of the chlorides[20] we observed a clear $^{TW}CCS_{N2}$ minimum for the cerium cluster and an increase between cerium, praseodymium and neodymium (see Fig. 3 and Table S1 in that paper). In this case, according to the calculations, the three strictly analogous chloride isomers are even closer in energy for the early lanthanides and consequently the relative amounts of isomers **B** and **C** were larger.[20]

$Ln_6Br_{19}^-$. The hexamer clusters reveal a behaviour that does not show in any of the other clusters. As can be seen from Fig. 2 for most Ln we observe two peaks in the arrival time distributions that differ in cross section by *ca.* 2%. For the early lanthanides the first peak dominates. Both peaks are seen for $Pr_6Br_{19}^-$ but with a unique (dynamic) behaviour which we will return to in a more specific discussion below (also of minor additional features in the $La_6Br_{19}^-$ and $Ce_6Br_{19}^-$ measurements, see chapter 3.3.2 and Fig. 10(a) and (b)). For $Nd_6Br_{19}^-$ both peaks are comparable in intensity, and from $Sm_6Br_{19}^-$ to $Lu_6Br_{19}^-$ the relative intensity of the first peak decreases from 26% to 7%. Qualitatively this is in line with our finding for the chlorides (i.e we observe two peaks with 2% CCS difference for

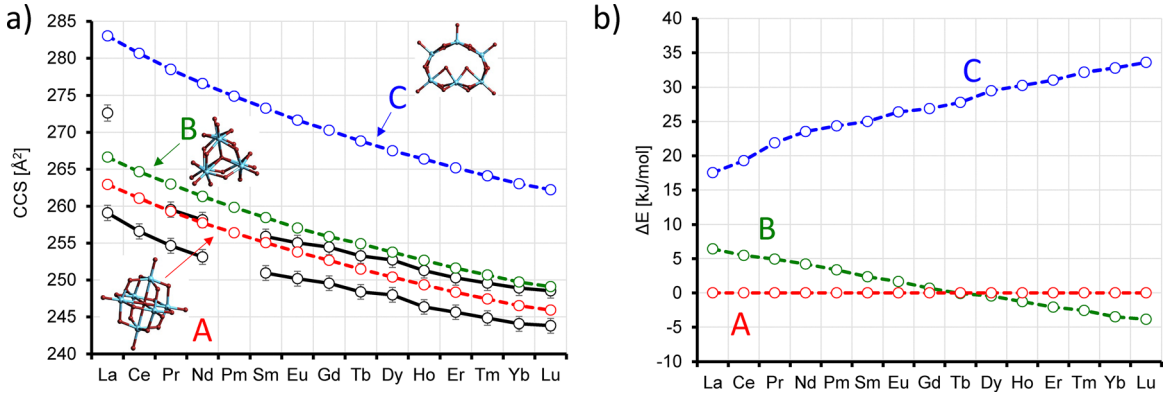

Fig. 9 (a) Experimental (black circles with error bars, $^{TW}CCS_{N2}$) and calculated (red, blue and green circles, $^{theo}CCS_{N2}$) collision cross sections for the three calculated isomers **A**, **B** and **C** of $Ln_6Br_{19}^-$. (b) Calculated (electronic) energy differences, taking isomers **A** as reference, zero-point energies not included.

both halides), however there is a significant difference in the relative intensities as function of the lanthanide: for the chlorides, the relative intensities of the two isomers cross later in the series, between dysprosium and holmium (see Table S1). So, while the isomer intensity ratio is 26% to 74% for $Sm_6Br_{19}^-$, it is 94% to 6% for $Sm_6Cl_{19}^-$.

The bimodal arrival time distributions are in line with the DFT calculations that predict two $Ln_6Br_{19}^-$ isomers **A** and **B** within 5 kJ mol^{-1} of each other. For the early lanthanides **A** is preferred, for the late **B**, see Fig. 9. Both isomers are very compact and consist of a central bromide surrounded by a shell of six Ln atoms (1 μ_6-Br, 12 μ_2-Br, 6 terminal), **A** is of O_h symmetry, **B** is of C_{3v} symmetry. The $^{theo}CCS_{N2}$ of **A** is *ca.* 1–2% above the first experimental peak, while $^{theo}CCS_{N2}$ of **B** agrees within 1% with the $^{TW}CCS_{N2}$ value of the second peak (note that based on our LJ-parameter calibration we expect a slight overestimation in the calculations, see above). A third isomer **C** is 17 kJ mol^{-1} above **A** for La, but the energy difference increases along the series to more than 30 kJ mol^{-1} for Lu. This isomer might be responsible for the small extra peak at 272.6 Å^2 that we observe for La, see Fig. 9 and 10(a) and more detailed discussion in 3.3.2 below.

3.3 Tracking isomer interconversion in $Ln_6Br_{19}^-$

A closer look at the hexamers reveals, in addition to the different relative intensities of the two isomers, further differences depending on the respective lanthanide. This can be seen when looking at the shape of the arrival time distributions as a function of the number of cycles, Fig. 10. Except for Ln = La, Ce and Pr, we were able to base-line resolve the two isomers of $Ln_6Br_{19}^-$ after more than 5 cycles of IMS separation. In addition we observed that their relative intensities did not change upon further cycling up to the maxmium accessible experimental timescale of *ca.* 400 ms (at larger timescales the faster isomer packet overtakes the slower isomer).

By contrast, for = La, Ce and Pr the relative isomer intensities vary with the number of cycles as can be seen by the decreasing intensity of the second peak (see Fig. 10(a)–(c) and Section 3.3.2).

We stress that for $Ln_6Br_{19}^-$, (Ln = Nd–Lu) and for the complete series of all previously studied $Ln_6Cl_{19}^-$ clusters showing two baseline separable isomers, the relative intensities do not substantially vary with the number of cycles. In the following, we will discuss these differences for each lanthanide in more detail.

3.3.1 $Nd_6Br_{19}^-$, $Sm_6Br_{19}^-$, $Eu_6Br_{19}^-$ and late lanthanides. We start our discussion with Nd–Lu, where the two isomers can be resolved within 5 cycles and for which the relative intensities then remain unchanged. We first address the question whether the isomer ratios (see Table 1) reflect their relative thermodynamic stabilities or are consequences of their ionisation/formation kinetics. To answer this, we used the IMS–IMS capabilities of our instrument – as in our previous lanthanide chloride cluster study. The experimental sequence was as follows: first the mass selected packet of "as-prepared" clusters underwent 5 cycles of IMS separation (in the cyclic trap = cIM stage of the apparatus) sufficient for base-line separation of the two isomers. Then, one of the isomers was pulse extracted from the cIM and transferred back into the pre-store (an RF-ion trap upstream from the cIM). Meanwhile the other isomer was discarded (ejected from the cIM). Thereafter, the first isomer (isomer **A**) was reinjected into the cIM with adjustable injection energy and the resulting isomer distribution was analysed for another 10 cycles. The result is shown in Fig. 11 for $Nd_6Br_{19}^-$ as an example. Upon isolating and reinjecting isomer **A** at nominally 0 eV injection energy, more than 95% of its relative ion intensity (*versus* isomer **B**) was still retained after nearly 400 ms. If we increase the injection energy to 50 eV, the relative intensity of isomer **A** drops to *ca.* 28% as isomer **B** is correspondingly formed (see Fig. 11(a) and (c)). If we isolate isomer **B** instead, its relative intensity drops from >95% at 0 eV injection energy to *ca.* 72% at 50 eV (Fig. 11(b) and (c)). With sufficient injection energy, we observe that the isomer ratio becomes independent of the choice of the isomer that is selected and reinjected – suggesting that a close to thermodynamic equilibrium situation has been attained. Note that up to *ca.* 60 eV injection energy, fragmentation (*via* loss of neutral $LnBr_3$) is negligible. In Table 2 and

Fig. S3 we summarize the results for the other $Ln_6Br_{19}^-$ clusters (Nd–Lu) and compare them with the ''as-prepared'' isomer ratio emanating from the cluster ion source: in all cases, isomer **B** dominates the distribution, independent of the prehistory. The numbers vary slightly (between ''from source'' and ''isomer selected''), implying that thermodynamic equilibrium at a common vibrational temperature is almost, but not perfectly reached.

3.3.2 Early lanthanides: $La_6Br_{19}^-$, $Ce_6Br_{19}^-$ and $Pr_6Br_{19}^-$. Next, we focus on the early lanthanides La, Ce, Pr – for which relative isomer intensity of as-prepared clusters changes with the number of cycles (without collisional excitation).

$La_6Br_{19}^-$. As can be seen in Fig. 10(a), the 1 to 5 cycle mobilograms obtained for as-prepared $La_6Br_{19}^-$ resolve a small additional peak that is initially present in the 1-cycle

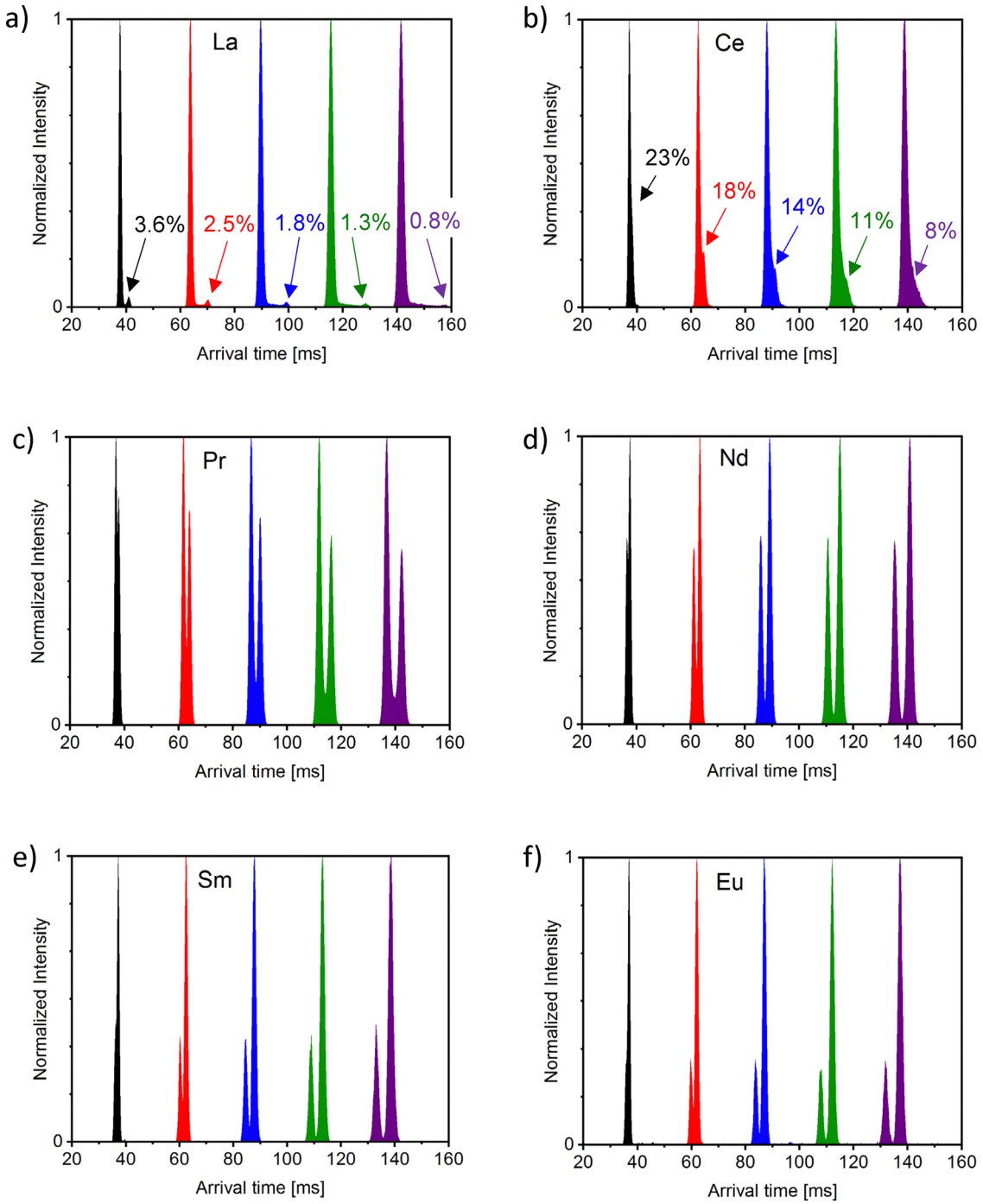

Fig. 10 Arrival time distributions of $Ln_6Br_{19}^-$ anions (Ln = La, Ce, Pr, Nd, Sm, Eu) after 1 (black), 2 (red), 3 (blue), 4 (green) and 5 (purple) cycles, respectively. (a) La, (b) Ce, (c) Pr, (d) Nd, (e) Sm and (f) Eu.

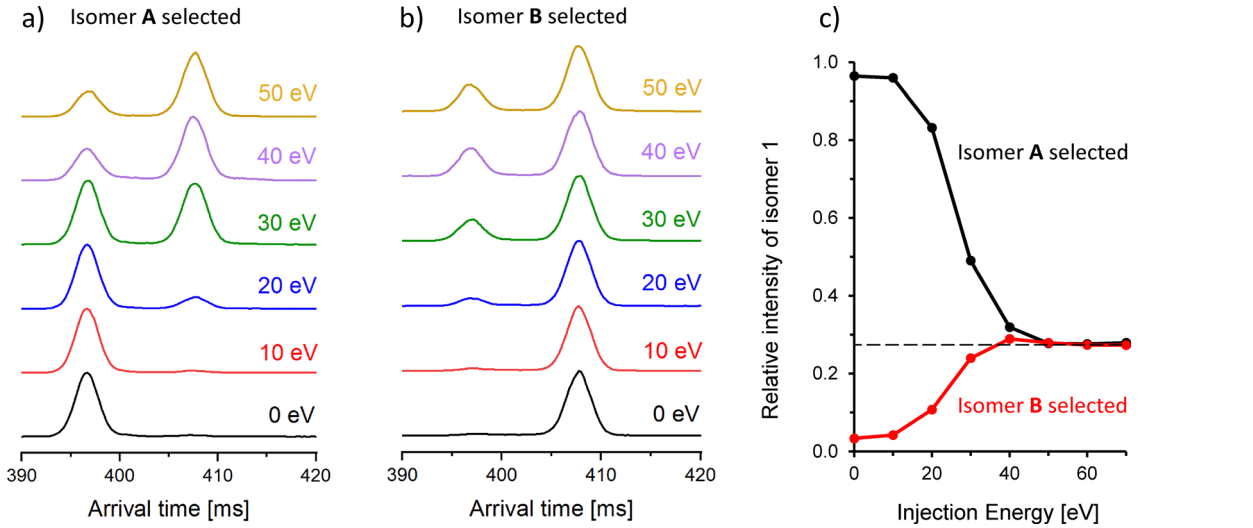

Fig. 11 IMS–IMS experiment for $Nd_6Br_{19}^-$: (a) The first peak of the arrival time distribution (isomer 1 shown after 5 cycles of separation) is selected, transferred into the pre-store, reinjected with variable kinetic energy and separated for another 10 cycles, (b) same workflow with second peak selected (isomer 2), (c) isomer ratio as function of injection energy; note that it is the same for either prehistory (a) or (b).

Table 2 Relative intensity of isomer **A**, either obtained directly from the ESI source or *via* selection of either isomer **A** or **B** and reinjection from pre-store with 60 eV of injection energy

	From source (%)	Isomer **A** selected (%)	Isomer **B** selected (%)
Nd	46	28	28
Sm	26	19	18
Eu	27	19	17
Gd	19	17	16
Tb	16	16	13
Dy	13	17	11
Ho	11	14	9
Er	10	19	9
Tm	8	12	7
Yb	8	16	6
Lu	7	12	6

measurement but no longer observable after 10 cycles, Fig. 2. In contrast to all other $Ln_6Br_{19}^-$, it is readily separable in just one cycle, *i.e.* its CCS is much larger than that of the main peak (assigned to isomer **A**, see Fig. 9). After calibration, we obtain a $^{TW}CCS_{N2}$ of 272.6 Å^2, *i.e.* 5% larger than the $^{TW}CCS_{N2}$ of the main peak (259.1 Å^2). We assign this minor peak to isomer **C**, see Fig. 9. Interestingly, its relative intensity quickly decreases with the number of cycles, from 3.6% (1 cycle) to 0.8% (5 cycles) (see Fig. 10(a)) to immeasurably small (10 cycles). Furthermore, the main peak also shows some tailing to longer arrival times, in line with an isomer with *ca.* 2% larger CCS having $<2\%$ relative intensity (most likely isomer **B**). Together these findings suggest that three isomers are originally present, one (**A**) clearly dominates and the other two (**B** and **C**) convert into the dominating isomer on a 100 ms time scale. As a corollary, our observations suggest that the isomer distribution is still evolving upon insertion of the corresponding as-prepared ion packet into the cIM stage.

$Ce_6Br_{19}^-$. For $Ce_6Br_{19}^-$, the well separated peak with 5% larger CCS is missing, but the tailing of the main peak is more obvious (see Fig. 10(b)) than for $La_6Br_{19}^-$. The shoulder in the 1-cycle measurement accounts for *ca.* 23% relative intensity. It decreases to below 10% after 5 cycles (as quantified by fitting two Gaussians to main peak and shoulder, see Fig. S4). At 10 cycles the shoulder has vanished within the background. Based on the position of the shoulder, we obtain a CCS of 260.5 Å^2, *ca.* 4 Å^2 (1.5%) larger than the main peak, as expected for isomer **B**. Again, these findings suggest an interconversion from isomer **B** to **A** during the ion mobility measurement and we estimate the **B** → **A** isomerisation rate constant to *ca.* 10 s^{-1}.

$Pr_6Br_{19}^-$. Isomer (inter)conversion on the measurement timescale is even more obvious for praseodymium. As can be seen in Fig. 12, the second peak in the arrival time distribution, isomer **B**, slowly decreases in relative intensity from *ca.* 85% of the main peak, isomer **A**, after 1 cycle to *ca.* 30% after 15 cycles. Furthermore, even after 15 cycles the two peaks are not baseline resolved, although the instrumental resolution is more than sufficient for this.

There was no significant fragmentation to charged ionic products under these conditions. Electron autodetachment would require surmounting prohibitively high electron affinities of more than 300 kJ mol^{-1} and is therefore highly unlikely. Also, ion scattering loss during cIM passage is minor and in particular it is non-specific for ions having close lying CCS like the isomers studied here (*ca.* 2% loss per cycle has been reported in ref. 17). Consequently, the relative intensity decay of isomer **B** must be due to it slow transformation into isomer A. The overall shape of the arrival time distribution, especially the filling of the gap between the two peaks is due to ions that spend a part of their drift time as isomer **A** and some of the rest of their time as isomer **B**, resulting in an

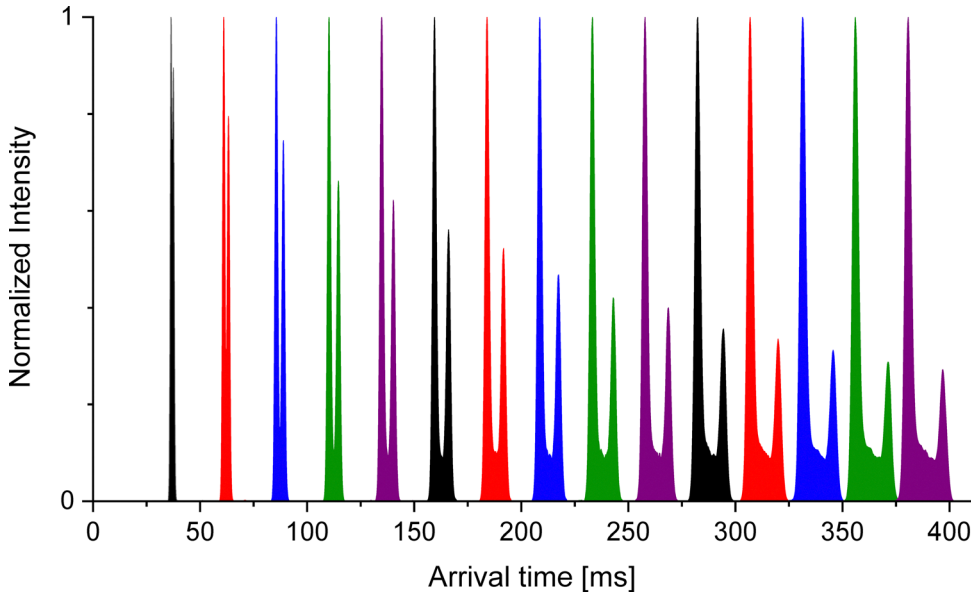

Fig. 12 Arrival time distributions of $Pr_6Br_{19}^-$ after 1–15 cycles. Note that at around 15 cycles the arrival time distribution fills the complete cycle and the faster isomer **A** starts to pass the slower isomer **B**.

intermediate drift time. In order to disentangle the interconversion kinetics, we used the capability of the Cyclic instrument to remove a slice of the arrival time distribution from the cycle without perturbing the isomer ion of interest. The experimental workflow is as follows: first, after injection, we performed 5 cycles of separation sufficient to resolve both isomers, then we removed the intermediate ions as well as isomer **B**, *i.e.* we kept only the narrow slice corresponding to those isomer **A** species which had not yet undergone any isomerization. Next, we performed another 1, 2, … 15 cycles of separation. With increasing number of cycles a tailing behind the peak develops that corresponds to ions that have transferred into isomer **B** during the drift time. (Note that even if some of these species would then convert back to isomer **A** before detection they would still arrive in the tail). The reverse reaction (isomer **B** → isomer **A**) was analysed in a similar manner, by removing the drift time slice corresponding to isomer **A** after 5 cycles of separation. The mobilograms obtained with the two experimental sequences are shown in Fig. 13(a) and (b) respectively (note that this procedure was not possible for $Ce_6Br_{19}^-$ due to the fast decay of isomer **B**, it disappeared before it could be resolved). As can be seen from the tailing in Fig. 13(a) isomer **A** reacts to isomer **B**, the growing leading shoulder observed in Fig. 13(b) corresponds to the reverse reaction. The slow reappearance of the initially removed isomer is also illustrated in Fig. S5 with the arrival time distributions shifted to match the position of the respective selected isomer.

To determine the isomerization rate constants, the data can be analysed quantitatively, by comparing the relative areas of the peak and the respective shoulder. The peak corresponds to ions that have not isomerized during the drift time while the shoulder corresponds to ions that have isomerized at least once. A simple kinetic analysis (see Fig. S6 and Table S8) reveals first order rate constants of $k_{\mathbf{A}\rightarrow\mathbf{B}} = 0.2\ s^{-1}$ for **A** → **B** and $k_{\mathbf{B}\rightarrow\mathbf{A}} = 1.8\ s^{-1}$ for **B** → **A** (*i.e.* more than fivefold slower than the **B** → **A** isomerisation rate constant of *ca.* $10\ s^{-1}$ estimated in the $Ce_6Br_{19}^-$ case). For $Nd_6Br_{19}^-$ the interconversion was basically absent on the time-scale of our experiment (see Fig. S7).

This raises the question of why we see isomer interconversion during the IMS separation for the early lanthanide bromide hexamers $La_6Br_{19}^-$, $Ce_6Br_{19}^-$ and $Pr_6Br_{19}^-$, but not for the other $Ln_6Br_{19}^-$ clusters and not at all for the lanthanide chloride hexamers $Ln_6Cl_{19}^-$? As can be seen in Fig. S2 the energy barrier between hexamer isomers **A** and **B** strongly increases along the lanthanide bromide series from 75 kJ mol^{-1} for $La_6Br_{19}^-$, 76 kJ mol^{-1} $Ce_6Br_{19}^-$, 83 kJ mol^{-1} for $Pr_6Br_{19}^-$, 86 kJ mol^{-1} for $Nd_6Br_{19}^-$ to finally 121 kJ mol^{-1} for $Lu_6Br_{19}^-$ (in this case reverse barriers are roughly the same as forward barriers because isomers "**A**" and "**B**" are calculated to be within 5 kJ mol^{-1} of each other). The barrier heights for the lanthanide chlorides are all higher, starting at 83 kJ mol^{-1} for $La_6Cl_{19}^-$. So, for a 25-atom $Ln_6Br_{19}^-$ at room temperature, barrier heights around 80 kJ mol^{-1} appear to correspond to a unimolecular isomerization time scale that is very near to the lower limit but still within the overall time window of our experiment (*ca.* 1 s).

4. Summary and conclusions

Cyclic IMS–MS measurements together with DFT calculations and trajectory method simulations of collision cross sections has been used to explore the structures, energetically low-lying isomer space and isomer interconversion of isolated $Ln_xBr_{3x+1}^-$ for $x \leq 6$ and all Ln = La⋯ Lu (except Pm). We probed primarily

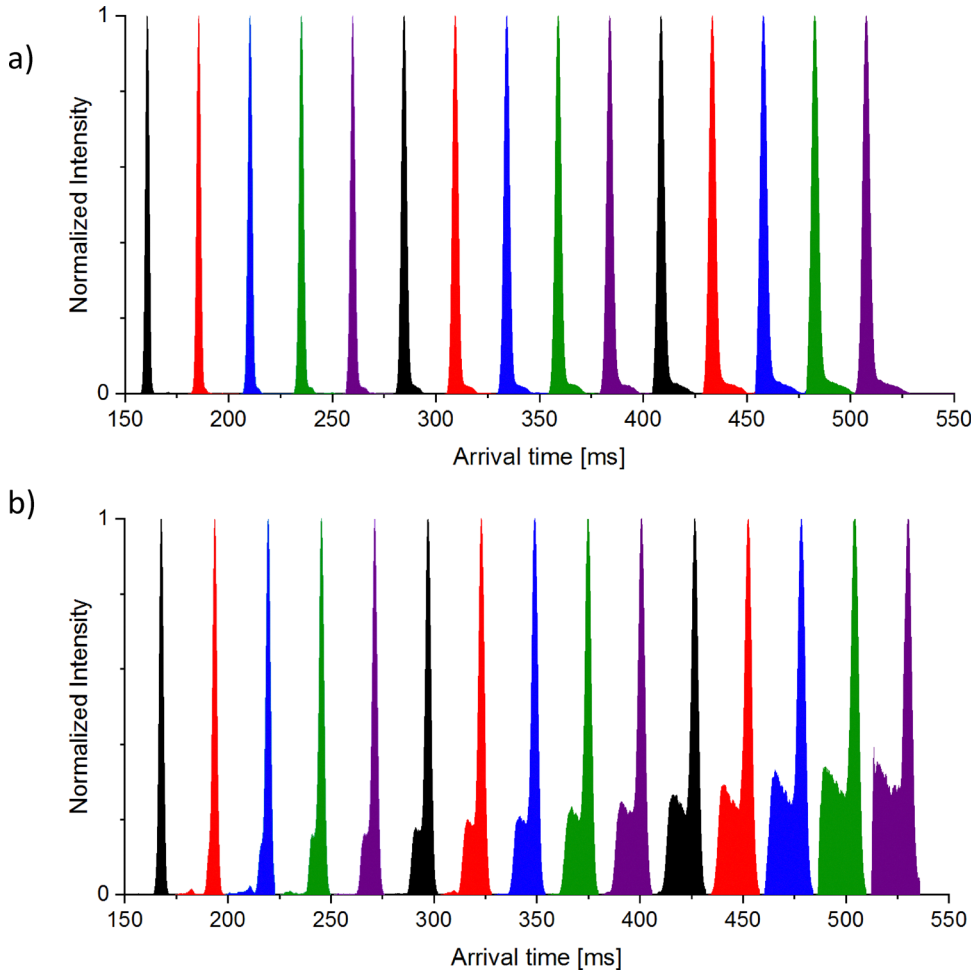

Fig. 13 Arrival time distributions of $Pr_6Br_{19}^-$ after isomer separation. Experimental sequences (a) 5 cycles separation – removal of isomer **B** – 1 to 15 cycles separation, (b) 5 cycles separation – removal of isomer **A** – 1 to 15 cycles separation.

m/*z*-selected species thermalized to near room temperature although collisional annealing was also applied in several cases. Similar to our recent work for $Ln_xCl_{3x+1}^-$ ($x \leq 6$),[20] the 70 $Ln_xBr_{3x+1}^-$ anions studied can be categorized into two groups: small clusters ($x \leq 5$) many of which show isomer interconversion on a faster than experimental timescale (notably all Ln_2Br_7, all Ln_4Br_{13} and Ln_5Br_{16} (La and Ce)) and larger species (all $x = 6$) showing enhanced structural rigidity on the experimental timescale and correspondingly slower isomer interconversion dynamics.

For all $Ln_xBr_{3x+1}^-$ the lowest energy structures predicted in DFT calculations were consistent with the IMS experiments. Much like $Ln_xCl_{3x+1}^-$, these structures reflect ionic bonding with very limited directionality. They consequently comprise Ln(III) centres bridged (and terminated) by multiple bromides. Ring and chain motifs are observed to be the lowest energy forms for the smaller clusters. These give way for larger clusters to more compact three-dimensional structures. At cluster sizes with two or more close lying isomers, the lanthanide contraction again leads to systematic changes in structure types across the Ln series. However, the corresponding crossing points (at which the energetic ordering of isomers inverts) vary between lanthanide bromide and chloride cluster anions – due to the different ionic radii and polarizabilities of Cl^- *versus* Br^-.

The phenomena observed experimentally for $Ln_6X_{19}^-$, differed in two decisive aspects between halides:

(i) For as-prepared $Ln_6Cl_{19}^-$, only one isomer was seen for Ln = La–Nd whereas Sm–Lu showed two baseline-separable isomers. By contrast, for $Ln_6Br_{19}^-$ the presence of at least two isomers could be inferred for all Ln.

(ii) In the case of $Ln_6Cl_{19}^-$, baseline separable isomers (which showed no interconversion on the 100 ms timescale at room temperature) could be interconverted by collisional annealing. By contrast for $Ln_6Br_{19}^-$, Ln = La, Ce and Pr, we observed spontaneous isomer (inter)conversion occurring on the experimental timescale without any additional excitation. In the case of $Pr_6Br_{19}^-$ we were able to measure the corresponding forward and reverse unimolecular isomerization rate constants.

An experimental determination of (different) forward and reverse thermal isomerization rate constants for a comparatively large isolated molecular ion as shown here for $Pr_6Br_{19}^-$ is

very unusual and perhaps the first of its kind. Admittedly, it is a fortuitous result which reflects the choice of a system with a fine enough intrinsic tuning raster (of cluster size and Ln/X composition) such that a cluster can be prepared with isomerization rate constants fitting well enough into the experimental time window of 100–300 ms such that their absolute values can be determined to reasonable accuracy. From these unimolecular isomerization rate constants for $Pr_6Br_{19}^-$ we can calculate an equilibrium constant: $K = N_{\text{isomer A}}/N_{\text{isomer B}} = k_{\mathbf{B}\rightarrow\mathbf{A}/\mathbf{1A}\rightarrow\mathbf{B}} = 1.8\ s^{-1}/0.2\ s^{-1} = 9$ for the reaction Isomer **A** ↔ Isomer **B** (assuming no other competing processes). At a temperature of 300 K, this corresponds by way of $RT \ln K = \Delta G$ to a free energy difference between the two interconverting $Pr_6Br_{19}^-$ isomers of *ca.* 5.5 kJ mol^{-1}. Interestingly, this number is close to the energy difference of 4.9 kJ mol^{-1} between isomers **A** and **B** from our DFT calculations (as outlined previously we do not compare to the calculated 300 K free energy difference because it is subject to large errors due to anharmonic low energy vibrations). This in turn supports the argument that the ions being probed under our experimental conditions have a common temperature.

Have they also reached an equilibrium isomer distribution? For this we return briefly to Fig. 12. After one cycle, the earliest time at which we can resolve isomers, the isomer ratio is nearly one, *i.e.* still a good distance away from the expected equilibrium ratio, $K = N_{\text{isomer A}}/N_{\text{isomer B}} = 9$. With increasing numbers of cycles the isomer ratio does develop exponentially towards a consistent limiting value – but apparently isomerization equilibrium has still not been completely reached before isomer **A** begins to overtake isomer **B** in the ring (and the measurement window closes). Presumably a different (higher?) effective source region temperature and/or the kinetics/thermodynamics of desolvation have contributed to an isomer starting ratio differing from that expected for the room temperature reaction equilibrium. In future work it would be interesting to study how spray conditions modify the initial ratio. It would also be informative to systematically vary the effective temperature of isolated $Pr_6Br_{19}^-$ (on a different instrumental platform allowing for T-dependent IMS measurements). Heating to 400 K should for example measurably shift the $Pr_6Br_{19}^-$ equilibrium constant from 9 to 5.2.

Of course, a finite number of isolated $Ln_6Br_{19}^-$ anions isomerizing back and forth under several mbar of N_2 collision gas can strictly speaking never be in thermodynamic equilibrium with a heat bath at 300 K. At this temperature a small fraction of the ion ensemble has enough internal energy to fragment (which is a common problem in mass spectrometry for studies of ions over long time scales).

One note in closing: it is amusing and perhaps instructive to relate the isomerization behaviour of $Ln_xBr_{3x+1}^-$ clusters to the Deborah number used to describe slow structural changes associated with several condensed phase phenomena, *e.g.* in the structural glass or polymer rheology fields.[37] Borrowing from their terminology, we define the "internal" timescale on which isomerization occurs in our isolated anions as $T_{\text{int}}^{\text{isom}}$ and the minimum "external" timescale on which an IMS measurement can determine changes to isomer composition as T_{ext}. The ratio of internal to external timescales corresponds to the Deborah number,[38] $D = T_{\text{int}}^{\text{isom}}/T_{\text{ext}}$. In our study we find $D \ll 1$ for many if not all clusters with $n \leq 5$, whereas the $Ln_6Br_{19}^-$ hexamers present a bouquet of Deborah numbers, having values ranging from near unity for Ln = La, Ce and Pr to $D > 1$ for Ln = Sm–Lu. The latter hexamers (like the lanthanide chlorides) only visit a subset of the overall phase space available to them during the experimental time window which can range up to 1s. It will be interesting (but challenging) to perform accurate multiscale molecular dynamics simulations of such systems which will need to describe both the individual molecular vibrations as well as their collective funnelling into isomer (inter)conversion over time ranges sufficiently long to ensure ergodicity.

Conflicts of interest

There are no conflicts of interest to declare.

Data availability

Most of the experimental data has been reported in the main text. Supplementary information: details of IMS^2 experiments and isomer interconversion studies and of the quantum chemical calculations including coordinates (for La), employed basis sets. See DOI: https://doi.org/10.1039/d5cp03530a.

The raw data of the MS and IMS experiments are available at RADAR4Chem DOI: https://doi.org/10.22000/9ha14qg0wjpjhx70.

Acknowledgements

MK, FW and PW gratefully acknowledge support of the German Science Foundation (DFG) as administered by the Collaborative Research Center 1573 "4f-for-future" in projects A2, C3 and Q. MK and PW are also grateful to DFG and KIT for the funding of a Cyclic IMS–MS instrument under Art. 91b GG. YN acknowledges funding of a six-month research stay in Karlsruhe by "GP-Chem" the International Joint Program in Integrated Chemistry of Tohoku University.

References

1 G. Egloff, M. Herrman, B. L. Levinson and M. F. Dull, Thermal Reactions of Terpene Hydrocarbons, *Chem. Rev.*, 1934, **14**, 287–383.
2 R. E. Fuguitt and J. E. Hawkins, Rate of the Thermal Isomerization of α-Pinene in the Liquid Phase1, *J. Am. Chem. Soc.*, 1947, **69**, 319–322.
3 Z. J. Xu, J. J. Han, C. Y. Zhang and H. X. Lou, The ballet of nature: the interconvertible isomerisation of natural products, *Nat. Prod. Rep.*, 2025, **42**, 1548–1578.
4 M. T. Bowers, P. R. Kemper, G. von Helden and P. A. M. van Koppen, Gas-Phase Ion Chromatography - Transition-Metal

State Selection and Carbon Cluster Formation, *Science*, 1993, **260**, 1446–1451.
5 G. von Helden, M. T. Hsu, P. R. Kemper and M. T. Bowers, Structures of Carbon Cluster Ions from 3 to 60 Atoms – Linears to Rings to Fullerenes, *J. Chem. Phys.*, 1991, **95**, 3835–3837.
6 M. F. Jarrold and V. A. Constant, Silicon Cluster Ions - Evidence for a Structural Transition, *Phys. Rev. Lett.*, 1991, **67**, 2994–2997.
7 N. Geue, G. A. Timco, G. F. S. Whitehead, E. J. L. McInnes, N. A. Burton, R. E. P. Winpenny and P. E. Barran, Formation and characterization of polymetallic $\{Cr_xM_y\}$ rings in vacuo, *Nat. Synth.*, 2023, **2**, 926–936.
8 P. Su, X. Zhu, S. M. Wilson, Y. N. Feng, H. Y. Samayoa-Oviedo, C. Sonnendecker, A. J. Smith, W. Zimmermann and J. Laskin, The effect of host size on binding in host-guest complexes of cyclodextrins and polyoxometalates, *Chem. Sci.*, 2024, **15**, 11825–11836.
9 P. Chakraborty, M. Neumaier, J. Seibel, N. Da Roit, A. Böttcher, C. Schmitt, D. Wang, C. Kübel, S. Behrens and M. M. Kappes, Exploring the Activation of Atomically Precise $Pt_{17}(CO)_{12}(PPh_3)_8^{2+}$ Clusters: Mechanism and Energetics in Gas Phase and on an Inert Surface, *ACS Nano*, 2025, **19**, 3624–3634.
10 F. Hennrich, S. Ito, P. Weis, M. Neumaier, S. Takano, T. Tsukuda and M. M. Kappes, Cyclic ion mobility of doped $[MAu_{24}L_{18}]^{2-}$ superatoms and their fragments (M = Ni, Pd and Pt; L = alkynyl), *Phys. Chem. Chem. Phys.*, 2024, **26**, 8408–8418.
11 P. Chakraborty, S. Malola, P. Weis, M. Neumaier, E. K. Schneider, H. Häkkinen and M. M. Kappes, Tailoring Vacancy Defects in Isolated Atomically Precise Silver Clusters through Mercury-Doped Intermediates, *J. Phys. Chem. Lett.*, 2023, **14**, 11659–11664.
12 I. Gatland, *Case Stud. At. Phys.*, 1974, **4**, 369–437.
13 R. R. Hudgins, P. Dugourd, J. M. Tenenbaum and M. F. Jarrold, Structural transitions in sodium chloride nanocrystals, *Phys. Rev. Lett.*, 1997, **78**, 4213–4216.
14 P. Weis, T. Bierweiler, E. Vollmer and M. M. Kappes, Au_9^+: Rapid isomerization reactions at 140 K, *J. Chem. Phys.*, 2002, **117**, 9293–9297.
15 S. Poyer, C. Comby-Zerbino, C. M. Choi, L. MacAleese, C. Deo, N. Bogliotti, J. Xie, J. Y. Salpin, P. Dugourd and F. Chirot, Conformational Dynamics in Ion Mobility Data, *Anal. Chem.*, 2017, **89**, 4230–4237.
16 R. Ito, X. He, K. Ohshimo and F. Misaizu, Large Conformational Change in the Isomerization of Flexible Crown Ether Observed at Low Temperature, *J. Phys. Chem. A*, 2022, **126**, 4359–4366.
17 K. Giles, J. Ujma, J. Wildgoose, S. Pringle, K. Richardson, D. Langridge and M. Green, A Cyclic Ion Mobility-Mass Spectrometry System, *Anal. Chem.*, 2019, **91**, 8564–8573.
18 R. B. Jordan, Lanthanide Contraction: What is Normal?, *Inorg. Chem.*, 2023, **62**, 3715–3721.
19 M. Lukanowski and F. Weigend, manuscript in preparation.
20 Y. Nakajima, P. Weis, F. Weigend, M. Lukanowski, F. Misaizu and M. M. Kappes, Lanthanide chloride clusters, $LnxCl_3x_{+1}^-$, x = 1–6: an ion mobility and DFT study of isomeric structures and interconversion timescales, *Phys. Chem. Chem. Phys.*, 2025, **27**, 1017–1030.
21 Turbomole, Version 7.9 2024; a development of University of Karlsruhe and Forschungszentrum Karlsruhe GmbH 1989-2007, Turbomole GmbH, since 2007; available via https://www.turbomole.org.
22 M. Sierka, J. Döbler, J. Sauer, G. Santambrogio, M. Brümmer, L. Wöste, E. Janssens, G. Meijer and K. R. Asmis, Unexpected structures of aluminum oxide clusters in the gas phase, *Angew. Chem., Int. Ed.*, 2007, **46**, 3372–3375.
23 J. P. Perdew, K. Burke and M. Ernzerhof, Generalized gradient approximation made simple, *Phys. Rev. Lett.*, 1996, **77**, 3865–3868.
24 M. Dolg, PhD thesis, University of Stuttgart, Germany, 1989.
25 A. Bergner, M. Dolg, W. Küchle, H. Stoll and H. Preuss, *Ab initio* energy-adjusted pseudopotentials for elements of groups 13–17, *Mol. Phys.*, 1993, **80**, 1431–1441.
26 M. Dolg, H. Stoll, A. Savin and H. Preuss, Energy-adjusted pseudopotentials for the rare-earth elements, *Theor. Chim. Acta*, 1989, **75**, 173–194.
27 M. Dolg, H. Stoll and H. Preuss, A combination of quasi-relativistic pseudopotential and ligand-field calculations for lanthanoid compounds, *Theor. Chim. Acta*, 1993, **85**, 441–450.
28 F. Weigend and R. Ahlrichs, Balanced basis sets of split valence, triple zeta valence and quadruple zeta valence quality for H to Rn: Design and assessment of accuracy, *Phys. Chem. Chem. Phys.*, 2005, **7**, 3297–3305.
29 O. Treutler and R. Ahlrichs, Efficient molecular numerical-integration schemes, *J. Chem. Phys.*, 1995, **102**, 346–354.
30 P. Plessow, Reaction Path Optimization without NEB Springs or Interpolation Algorithms, *J. Chem. Theory Comput.*, 2013, **9**, 1305–1310.
31 V. Gabelica, A. A. Shvartsburg, C. Afonso, P. Barran, J. L. P. Benesch, C. Bleiholder, M. T. Bowers, A. Bilbao, M. F. Bush, J. L. Campbell, I. D. G. Campuzano, T. Causon, B. H. Clowers, C. S. Creaser, E. De Pauw, J. Far, F. Fernandez-Lima, J. C. Fjeldsted, K. Giles, M. Groessl, C. J. Hogan, S. Hann, H. I. Kim, R. T. Kurulugama, J. C. May, J. A. McLean, K. Pagel, K. Richardson, M. E. Ridgeway, F. Rosu, F. Sobott, K. Thalassinos, S. J. Valentine and T. Wyttenbach, Recommendations for reporting ion mobility Mass Spectrometry measurements, *Mass Spectrom. Rev.*, 2019, **38**, 291–320.
32 C. Larriba and C. J. Hogan, Ion Mobilities in Diatomic Gases: Measurement versus Prediction with Non-Specular Scattering Models, *J. Phys. Chem. A*, 2013, **117**, 3887–3901.
33 C. Larriba and C. J. Hogan, Free molecular collision cross section calculation methods for nanoparticles and complex ions with energy accommodation, *J. Comput. Phys.*, 2013, **251**, 344–363.
34 R. D. Shannon, Revised Effective Ionic-radii and Systematic Studies of Interatomic Distances in Halides and Chalcogenides, *Acta Crystallogr., Sect. A*, 1976, **32**, 751–767.

35 U. C. Singh and P. A. Kollman, An Approach to Computing Electrostatic Charges for Molecules, *J. Comput. Chem.*, 1984, **5**, 129–145.
36 S. M. Stow, T. J. Causon, X. Y. Zheng, R. T. Kurulugama, T. Mairinger, J. C. May, E. E. Rennie, E. S. Baker, R. D. Smith, J. A. McLean, S. Hann and J. C. Fjeldsted, An Interlaboratory Evaluation of Drift Tube Ion Mobility-Mass Spectrometry Collision Cross Section Measurements, *Anal. Chem.*, 2017, **89**, 9048–9055.
37 J. C. Mauro, P. K. Gupta and R. J. Loucks, Continuously broken ergodicity, *J. Chem. Phys.*, 2007, **126**, 11.
38 https://en.wikipedia.org/wiki/Deborah_number.